TELKOMNIKA Telecommunication, Computing, Electronics and Control
Vol. 18, No. 4, August 2020, pp. 2213~2223
ISSN: 1693-6930, accredited First Grade by Kemenristekdikti, Decree No: 21/E/KPT/2018
DOI: 10.12928/TELKOMNIKA.v18i4.14228

Detection of uveal melanoma using fuzzy and neural networks classifiers

Daniel F. Santos, Helbert E. Espitia
Facultad de Ingeniería, Universidad Distrital Francisco José de Caldas, Bogotá, Colombia

Article Info

Article history:

Received Sep 28, 2019
Revised Mar 4, 2020
Accepted Mar 27, 2020

Keywords:

Fuzzy Systems
Image processing
Neural networks
Uveal melanoma

ABSTRACT

The use of image processing is increasingly utilized for disease detection. In this article, an algorithm is proposed to detect uveal melanoma (UM) which is a type of intraocular cancer. The proposed method integrates algorithms related to iris segmentation and proposes a novel algorithm for the detection of UM from the approach of fuzzy logic and neural networks. The study case results show 76% correct classification in the fuzzy logic system and 96.04% for the artificial neural networks.

Corresponding Author:

Helbert E. Espitia,
Facultad de Ingeniería,
Universidad Distrital Francisco José de Caldas, Bogotá, Colombia.
Email: heespitiac@udistrital.edu.co

1. INTRODUCTION

The traditional image processing is used to solve problems like quality improvement, restoration, highlight features, among others. Currently, with the emergence of branches such as fuzzy logic and neural networks, image processing is also being used to address problems related to diseases. Among them is the uveal melanoma (UM), a subtype of ocular melanoma (OM) [1] a type of intraocular cancer that arises in the melanocytes of the coloured part of the eye (iris), circle of muscle tissue (ciliary body) or in the largest part of the uvea track (choroid) which is located beneath the retina in the back part of the eye. Mostly, ocular melanomas appear within the choroid and come from the melanocytes, which are the cells of the body that produce pigment [2]. Early diagnosis and local treatment are crucial since survival rates correlate with the size of the primary tumour. However, approximately 50% of patients will develop metastases with a survival rate of 6-12 months from diagnosis [3].

Using modern tools like ultrasonography, fluorescein angiography, and optical coherence tomography can significantly aid in diagnosis [4, 5], roughly 3 out of 4 people with ocular melanoma survive for at least 5 years. Survival rates tend to be better for cancer detection in earlier stages than for those in later stages. When cancer is confined to the eye, the relative survival rate at 5 years is around 80%. For people with eye melanomas that have spread to distant parts of the body, the 5-year relative survival rate is around 15% [6] and 1-year survival rate is 10% to 15% [7–9].

In related works, a large number of projects associated with the iris have been developed. There are two main applications: identification of people through unique patterns [10–12] and detection of diseases where Iridology is found, which is a branch of alternative medicine that is responsible for examining patterns,

colours, and other characteristics of the iris to determine the health of patients [13, 14]. For example [15], where the iris is employed for the detection of Alzheimer.

In [16] is shown how to detect diseases in the iris using the Gabor filter. Among the classified diseases are corneal oedema, iridotomies, and conjunctivitis. Moreover, in [17], through techniques of Iridology and the Watershed transform diseases are identified, reaching an accuracy of 87.5% in the detection of kidney problems. In [18], using unique iris features and advanced encryption standard (AES) images are encrypted, achieving high levels of security.

As shown in [2, 5] there is no approved therapy to treat metastatic uveal melanoma and considering that its early detection significantly increases the chances of survival, there was developed a method to identify UM. The proposed method integrates algorithms used in work related to iris segmentation and proposes a methodology for UM detection from the fuzzy logic and neural network approach, as well as present a variation of the algorithm proposed by Wildes in [19]. The variation implements additional logic to increase the accuracy as well as implementing data structures like a red-black tree and disjoint set with the union by rank and path compression to reduce the turnaround time.

The shown algorithm employed to detect UM consists of: 1) preprocess images with and without UM, 2) apply a segmentation algorithm to each of these preprocessed images to find the region of interest (ROI), 3) transform the ROI to another space that allows an analysis with less noise, 4) obtain descriptors of the ROIs to generate a training dataset, 5) a fuzzy and a neural network classifier are created based on the training dataset, and finally in 6) the results of the classifiers are analysed and compared.

2. IMAGE PROCESSING

Humans are very good at detecting patterns but unlike machines, we are not good at processing large amounts of data, then, if the machine is taught to identify patterns it is possible to automate many specialized tasks such as disease detection. For the present case study, Hough circular transform, adaptive binarizations, filters, Hu moments, among others techniques are used to train the classifiers to identify UM, a brief description of those algorithms is provided.

2.1. Hough circular transform

Hough circular transform (HCT) is an algorithm to search circles in images, this approach is used because it provides robustness to the presence of noise, occlusion and variation of illumination [20]. This algorithm has three fundamental phases:

1. Accumulator array computation
2. Center estimation
3. Radius estimation

The HCT is used to transform a set of characteristics of points in the space of the image, (1) to a set of votes accumulated in the space of the parameters (2). These votes are integer values that are stored in an array. The position of the arrangement that contains the most votes indicates the presence of a circle. The (1) represents a circle, where r is the radius and (x_0, y_0) are the coordinates of the centre of the circle.

$$r^2 = (x - x_0)^2 + (y - y_0)^2 \tag{1}$$

The (2) represents the parametrization of the circle where (x_0, y_0) are the coordinates of the centre of the circle and θ is the angle of inclination. That equation allows transforming a circle into a rectangle.

$$\begin{aligned} x &= x_0 + r\cos(\theta) \\ y &= y_0 + r\sin(\theta) \end{aligned} \tag{2}$$

2.2. Adaptive thresholding

Conventional thresholding methods use a threshold for all pixels, while adaptive thresholding (AT) changes the threshold value dynamically on the image. The AT has shown better results with respect to the traditional thresholding since the illumination and the shadows change depending on the position of the image [21]. Within the thresholding methods used in this article are: Gaussian thresholding (represented by (3)) and mean thresholding. In (4) is depicted an example of a Gaussian window.

$$h(u, v) = \frac{1}{2\pi\sigma^2} e^{-\frac{u^2+v^2}{2\sigma^2}} \tag{3}$$

$$H = \frac{1}{16}\begin{bmatrix}1 & 2 & 1\\ 2 & 4 & 2\\ 1 & 2 & 1\end{bmatrix} \quad (4)$$

2.3. Hu moments

The Hu Moments allow to obtain image features used in the classification process. The following definition is important in this regard.

Definition 1 *(Moment of an image): A measure that provides a generic representation of an object, with simple or complex figures [21].*

There are a considerable number of used and well-known moments within which we can include geometric moments [23], Zernike moments [24], rotational moments [25], and complex moments [26]. The invariants of the moment were introduced by Hu in [23], these are very useful properties that can be extracted from an image because they are not only independent to position, size and orientation but also to parallel projection, thus they have been widely used to perform pattern recognition, image registration and image reconstruction [23, 27–29].

2.4. Invariant moments

A two-dimensional moment of order $(p+q)$ is defined by the (5).

$$m_{pq} = \int_{-\infty}^{\infty}\int_{-\infty}^{\infty}(x)^p(y)^q f(x,y)dxdy \quad p,q = 0,1,2.. \quad (5)$$

If the function $f(x,y)$ is defined in parts, the moments of all orders exist and the sequence of moments m_{pq} is only determined by the function $f(x,y)$, but those moments in the (5) may not be invariant to translation, rotation or scale, thus the invariant Hu moments can be calculated using the central moments, which are defined by (6).

$$\mu_{pq} = \int_{-\infty}^{\infty}\int_{-\infty}^{\infty}(x-x')^p(y-y')^q f(x,y)dxdy \quad p,q = 0,1,2 \ldots \quad (6)$$

The moments μ_{pq} are calculated using the image $f(x,y)$, these are equivalent to m_{pq} whose centre has been moved to the centroid of the image, therefore, the moments are invariant to translation [23]. Where the pixel $f(x',y')$ is the centroid of the image and:

$$x' = \frac{m_{10}}{m_{00}}, \qquad y' = \frac{m_{01}}{m_{00}}$$

With the use of the normalization of the moments the invariance to scale can be obtained. This moment can be defined by:

$$n_{pq} = \frac{\mu_{pq}}{\mu_{00}^{\gamma}}, \qquad \gamma = \frac{p+q+2}{2}, \quad p+q = 2,3, \ldots \quad (7)$$

Based on those moments, Hu in [23] presented the seven moment invariants shown below:

$$\begin{aligned}
h_1 &= n_{20} + n_{02}\\
h_2 &= (n_{20} - n_{02})^2 + 4n_{11}^2\\
h_3 &= (n_{30} - 3n_{12})^2 + (3n_{21} - \mu_{03})^2\\
h_4 &= (n_{30} + n_{12})^2 + (n_{21} - \mu_{03})^2\\
h_5 &= (n_{30} - 3n_{12})(n_{30} + n_{12})[(n_{30} + n_{12})^2 - 3(n_{21} - n_{03})^2]\\
&\quad +(3n_{21} - n_{03})(n_{21} + n_{03})[3(n_{30} + n_{12})^2 - (n_{21} + n_{03})^2]\\
h_6 &= (n_{20} - n_{02})[(n_{30} + n_{12})^2 - (n_{21} + n_{03})^2]\\
&\quad +4n_{11}(n_{30} + n_{12})(n_{21} + n_{03})\\
h_7 &= (3n_{21} - n_{03})(n_{30} + n_{12})[(n_{30} + n_{12})^2 - 3(n_{21} - n_{03})^2]\\
&\quad -(n_{30} - 3n_{12})(n_{21} + n_{03})[3(n_{30} + n_{12})^2 - (n_{21} + n_{03})^2]
\end{aligned}$$

It is important to mention that the noise generated by different factors, such as the type of camera and file formatting, can produce errors when calculating moments. In other words, moments can vary with the geometric transformation of the image [29]. In the case of a scale transformation or rotation of the image, a rounding of pixel positions or interpolation is generated which causes that at a digital level the invariants of the moment also change [30].

3. RESEARCH METHOD

This section describes the algorithm (see Figure 1), each sub-section represents each stage as follows: the first one corresponds to the image processing; next, refers to the detection of the region of interest; afterwards comes the filtration and transformation of those regions to finally perform the feature extraction.

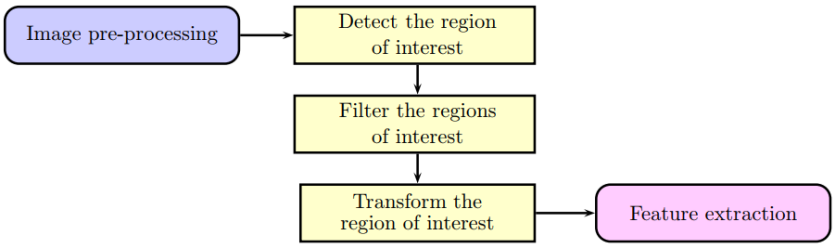

Figure 1. Stages for image feature extraction

3.1. Image pre-processing

This is the first phase and it is of vital importance to facilitate the detection of the ROI, in which enters an image $I(x,y)$ whose output is the image $M(x,y)$. Figure 2 shows the stages through which the image passes. Using Figure 3 it is shown how this stage works, this image corresponds to an eye affected with uveal melanoma [31]. The sequence of algorithms that facilitate the detection of the ROI:

- Grayscale transformation: First, an image with three channels RGB is received and transformed into a grayscale image; this is mainly due to the fact that a grayscale image is easier to process than an RGB image (see Figure 4).
- Apply median filter: The image is smoothed by applying a median filter, this will decrease the noise, helping to make the ROI clearer. The result of this process is shown in Figure 5.
- Apply binarization: With this stage the boundaries are clearly defined, the binarization used was the Adaptive Mean Thresholding and the Adaptive Gaussian Thresholding. Figure 6 shows the result obtained in this step.
- Image dilation: Again, a process is done to reduce noise, in this case, pepper type noise, using dilation. The respective result obtained in this step is shown in Figure 7.

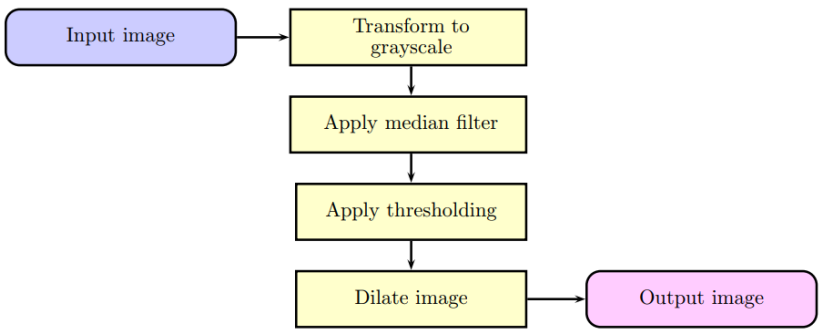

Figure 2. The sequence of algorithms that facilitate the detection of the ROI

Figure 3. Eye affected with uveal melanoma [31]

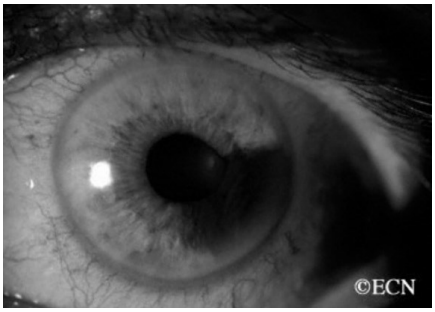

Figure 4. Image with UM converted to grayscale

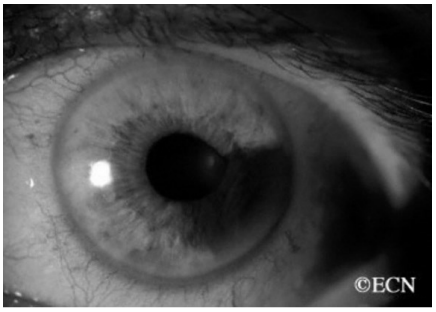

Figure 5. Image with UM in grayscale smoothed using a median filter

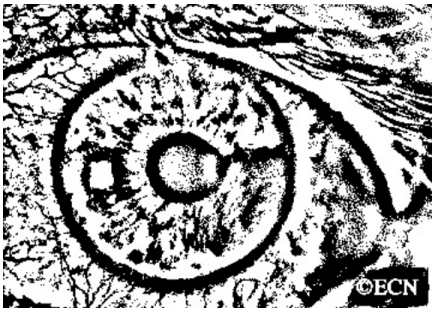

Figure 6. Image with UM after applying adaptive mean thresholding

Figure 7. Dilated image

3.2. Detection of the region of interest

The region of interest is the iris, this is also a crucial stage for the detection of UM since an inappropriate location of the ROI can result in extraction of characteristics from non-relevant parts, generating a training with noise and therefore an erroneous classification. Based on the literature of iris segmentation algorithms, it was decided to use a variation of the wildes algorithm due to its ease of implementation, computational efficiency and suitable properties.

- Algorithm of ROI detection

Algorithm 1 receives the image of Figure 7, calculates the width and height of the image to make an estimate of the maximum radius and minimum radius that the iris can have, the minimum is calculated based on a δ pre-established. As the function of the Hough transform receives as argument the image and the radius, this procedure is carried out within an iteration varying the $radius$ from $minRadius$ to $maxRadius$ and at the same time it is executed twice since two types of binarization are used. Because the algorithm is executed several times a set is used to store unique ROIs. The set stores the ROIs in a red-black tree that will allow to access the elements quickly and avoiding duplicates. At the end of this stage, there is a set of possible regions of interest, as seen in Figure 8.

Algorithm 1. Identify ROI

```
procedure DETECT(I(x, y))
        maxRadius ← min(width(I), height(I))
        minRadius ← maxRadius/δ
        circles ← { }
        for radius ← minRadius to maxRadius do
            circles.insert(houghTransform(I, radius))
        return circles
```

3.3. Filtering of regions of interest

As can be seen in Figure 8 a large number of regions of interest were detected, some valid and others not, some with noise or very similar, thus it is necessary a filtering stage. Reducing the number of ROIs reduces the processing stage. Algorithm 2 discards invalid circles. Since the performance of the algorithm deteriorates under uncontrolled conditions [19], and there is a large number of similar ROIs, Algorithm 3 was made to join similar ROI, this last one uses disjoint set with union by rank and path compression that by means of a δ of distance joins similar ROI. The results of this stage can be seen in Figure 9.

Algorithm 2. Filter (ROI)

```
procedure FILTER(regions)
        areaTotal ←(img.width*img.height)
        validRegions ← { }
        for region in regions do
            area ← (region.r)^2 * π
            ratio ← area/areaTotal
            if ratio is in interval [a, b]then
                if region is completely inside then
                    validRegions.insert(region)
        return validRegions                    ▷ The set with the valid regions
```

Algorithm 3. Join similar (ROI)

```
procedure JOIN(regions)
        UnionFind uf (regions.length)          ▷ Instance of Structure Union Find
        for i ← 0 to regions.length do
            for j ← i + 1 to regions.length do
                if dist(region_i, region_j) < delta then uf.unite(region_i, region_j)
        return uf.different_regions            ▷ The set with all differente regions after union process
```

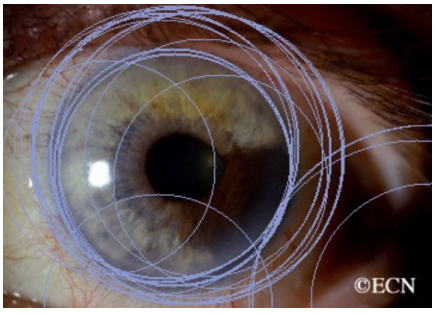

Figure 8. Possible regions of interest detected using Algorithm 1, obtained from the dilated images

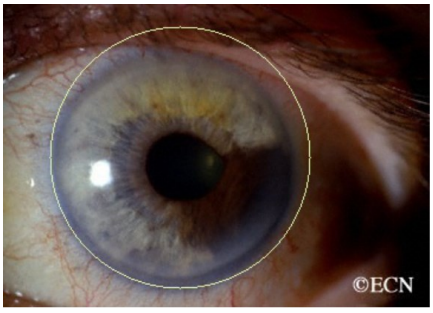

Figure 9. Regions of Interest filtered using Algorithms 2 and 3

3.4. Transformation of the region of interest

With the detection of the ROI it is applied a transformation that reduces noise in order to isolate the iris and to obtain the features. The scheme of Figure 10 was used to carry out the process of unwrapping the iris. The iris region is transformed into a confined rectangular area, recognizing the boundaries is possible to apply a transformation from Polar coordinates (r, θ) to Cartesian coordinates (x, y), according to (8) and (9), where $\theta \in [0, 2\pi], (x_p, y_p)$ represents the direction of the pupil region which is being transformed and (x_i, y_i) is the new location of that iris element. The results showed in Figures 11 and 12 display the filtered image and the transformation to Cartesian coordinates.

$$x_i = x_p + r\cos(\theta) \quad (8)$$

$$y_i = y_p + r\sin(\theta) \quad (9)$$

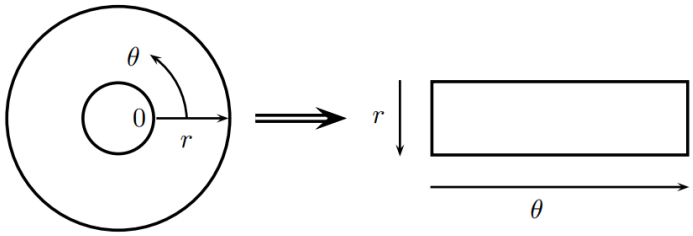

Figure 10. Scheme used for transform the region of interest

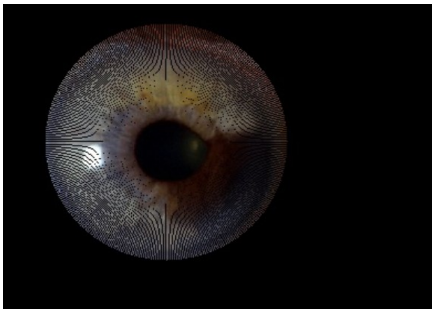

Figure 11. Region of interest isolated in Polar coordinates

Figure 12. Isolated region of interest in Cartesian coordinates

3.5. Feature extraction

For the features extraction, the Hu moments were selected due to their properties mentioned in detail in section 2.4. The extraction was performed in a total of 1622 images that are divided according to Table 1. With these images, the characteristics were extracted and stored in a comma-separated value (csv) file, which will be later used to train the classifiers.

Table 1. The number of images for feature extraction

Image	Number
Without Uveal Melanoma	1424
With Uveal Melanoma	198

3.6. Fuzzy model

The ranges that differentiate healthy and unhealthy iris sets are established using the data set (csv-file); with this processing, the membership functions were built in a Mamdani fuzzy system (Figure 13). Considering the seven Hu moments $h_1, h_2, h_3, h_4, h_5, h_6, h_7$ for each moment it was decided to use triangle functions to implement the antecedents shown in Figure 13, while Gaussian functions are implemented for the consequent; this represents a numerical value that identifies if the image is healthy or unhealthy, as shown in Figure 14. The result of this model can be seen in Table 2 in which it was obtained 76% of correct classification.

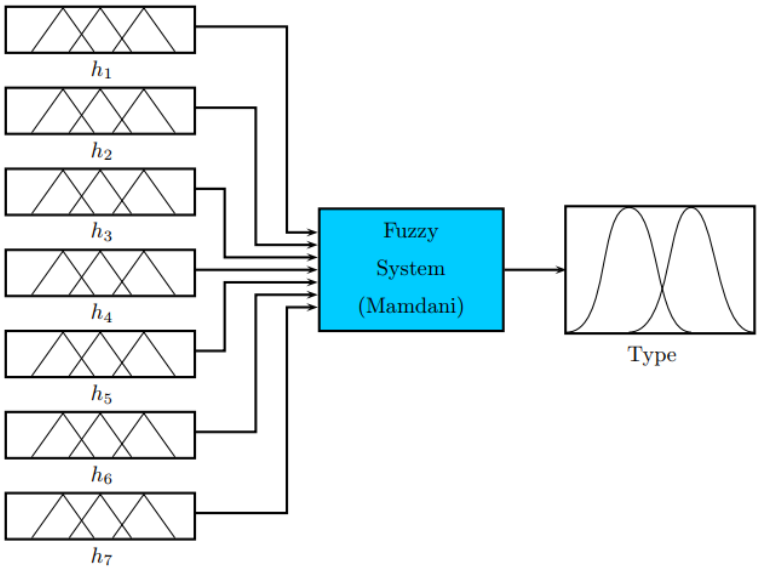

Figure 13. Block diagram of the fuzzy inference system

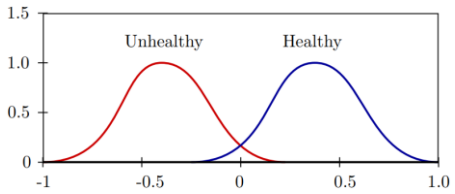

Figure 14. Fuzzy sets used in the output for healthy or unhealthy classification

3.7. Neural networks

Because the proposed fuzzy system has a success rate of 76%, it was decided to perform a neural network classifier. Supported by an experimental design; different configurations of neural networks were implemented to obtain the accuracy of the classifier. The neural networks parameters that are changed can be seen in Table 2. The inputs of the neural network are the seven Hu moments $h_1, h_2, h_3, h_4, h_5, h_6, h_7$ and the outputs are two: healthy and unhealthy. Figure 15 shows a sample configuration with 7 inputs, 2 hidden layers with 3 neurons each one and 2 outputs.

Table 2. Parameters and ranges that varied for the neural network test

Paramater	Range
Number Hidden Layers	[1, 10]
Number Neurons per layer	[1, 10]
Type of network	Feed forward, Cascade forward, Fitnet

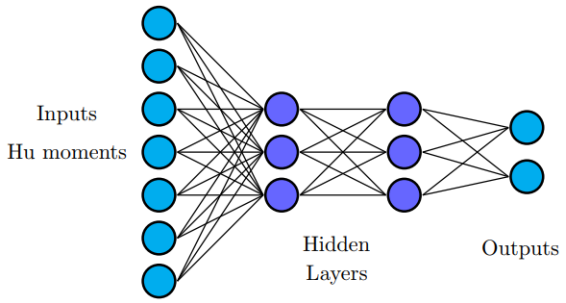

Figure 15. Sample configuration neural network

Below are the results with three types of neural networks, each configuration was executed four times, the results of one of the executions are shown below; finally, statistical measures are shown each configuration. Figure 16 represents the mean squared error (MSE) for each type of neural network, varying the number of layers and the number of neurons based on the parameters of Table 2. These graphs and Table 3 present the conditions in which the UM is most likely to be detected. The configurations with low MSE outcomes are the ones with less than 6 neurons per layer and less than 5 layers.

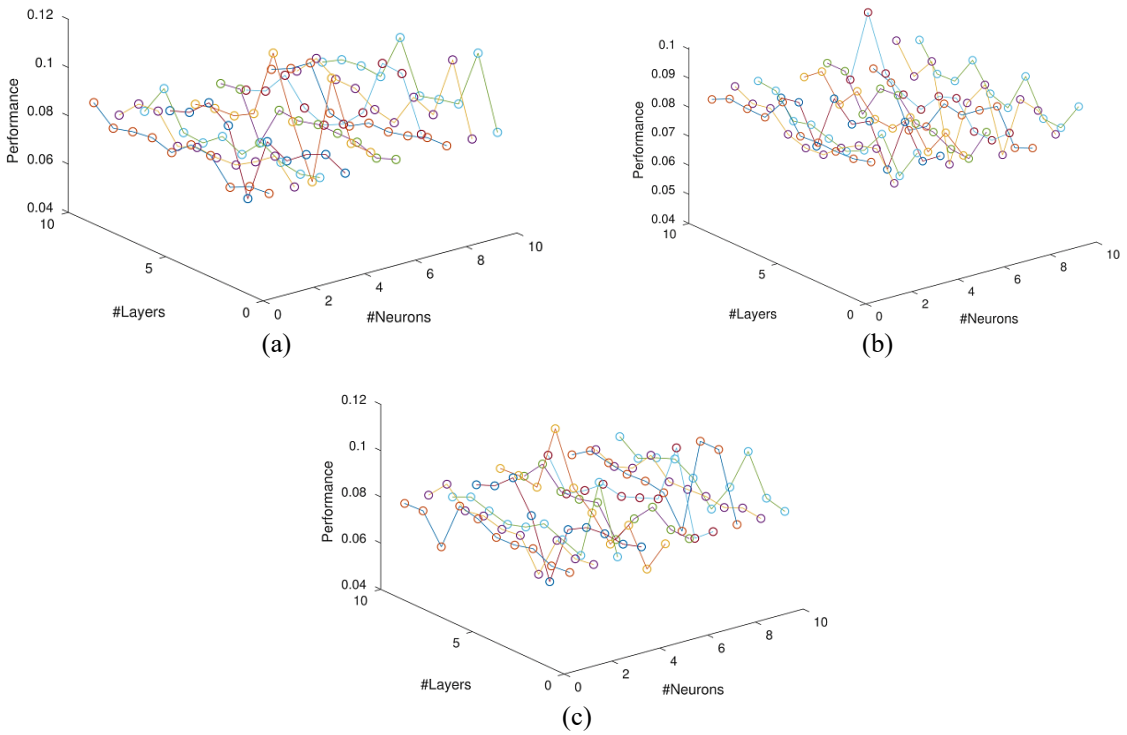

Figure 16. Neural networks results (a) performance feed forward net, (b) performance cascade forward net, (c) performance FitNet

Table 3. Results of neural network configurations

Type of Network		Results			
Feed Forward Net	Layers/Neurons	4	6	7	8
	4	0.0720	0.0491	0.0757	0.0814
	5	0.0606	0.1065	0.07783	0.0732
	6	0.0778	0.0756	0.0763	0.0592
	8	0.0728	0.0679	0.0696	0.0867
Cascade Forward Net	Layers/Neurons	2	4	7	8
	4	0.0751	0.0667	0.0828	0.0636
	6	0.0717	0.0753	0.0819	0.0824
	8	0.0712	0.0786	0.0647	0.0606
	9	0.08198	0.0611	0.0495	0.0822
FitNet	Layers/Neurons	4	5	6	8
	1	0.0783	0.0780	0.0823	0.0629
	2	0.0629	0.0760	0.0750	0.0757
	4	0.0775	0.0729	0.0467	0.0843
	6	0.0756	0.0630	0.0753	0.0728

4. RESULTS AND DISCUSSION

As an experimental result, the accuracy rates of the fuzzy system and the neural network system are shown. In the confusion matrix of Table 4 are shown the results of the fuzzy classifier, the function that was used to perform the classification can be seen in the (10) where F is the fuzzy system created, H is the function that obtains the values of Hu and I is the image to be tested. As can be seen in the confusion matrix of Table 4, the fuzzy system generates better results with healthy images. The hypothesis of these results is based on the fact that the entry dataset is larger for healthy iris than for unhealthy iris. Given the last

table is possible to compute some measures like accuracy, error rate, sensitivity and precision that can give more insights of the model, the results are 0.76633, 0.23366, 0.88847, and 0.83917, respectively. Regarding the precision and sensitivity can be shown that the system is prone to detect healthy images. After executing the different configurations of neural networks, a statistical analysis was performed on four data-sets corresponding to the results of each configuration; σ_i represents the standard deviation of the results of the execution number i. The results obtained are shown in Table 5, where it can be seen that the network that produces the best results is the feed forward network with a success rate of 96.04%.

$$C(I) = \begin{cases} if & F(H(I)) > 0 \quad healthy \\ if & F(H(I)) < 0 \quad unhealthy \end{cases} \tag{10}$$

Table 4. Confusion matrix using the proposed fuzzy system

	True diagnosis		
	Healthy	Unhealthy	Total
Healthy	1195	229	1424
Unhealthy	150	48	198
Total	1345	277	1622

Table 5. Standard deviation and MSE

Type of Network	σ_1	MSE_1	σ_2	MSE_2	σ_3	MSE_3	σ_4	MSE_4
Feed Forward	0.0093	0.0491	0.4598	0.0408	0.0080	0.0396	0.0098	0.0442
Cascade Forward	0.0066	0.0495	0.00110	0.0463	0.0095	0.0431	0.0238	0.0466
FitNet	0.0090	0.0467	0.0205	0.0445	0.0107	0.0446	0.0066	0.0432

Finally, judging from the results collected through the different executions, it can be seen that the feed forward network produces the best accuracy of 96.04% with standard deviation of 0.008 which can be improved from different approaches such as increasing the size of the data set, incrementing the number of descriptors, e.g Gabor descriptor or using other techniques, e.g ANFIS, convolutional networks or genetic algorithms.

5. CONCLUSION

The proposed methodology was tested using different configurations, the experimental results show that fuzzy logic and neural networks classifiers provide a suitable system to detect uveal melanoma, achieving 76% in the fuzzy classifier and for the neural network classifier which performs better with an accuracy of 96.04% using a Feed Forward Net. For the segmentation of the ROI it was proposed a new algorithm built over the principles of Wildes algorithm, this new algorithm was done to improve the success ratio of well-segmented regions of interest (ROIs) as well as the integration of data structures like disjoint-set with path and range compression to reduce the processing time. As a result of the pre-processing stage, it was possible to perform detection of the regions of interest. The stage of transformation and use of data structures was decisive to reduce the noise in the data set and the processing time for the feature extraction. In order to improve the performance of the classifiers, it is considered to expand the number of images used, as well as the integration of more descriptors into the training data set such as Gabor descriptors. In a future work the methodology and the algorithm proposed could be implemented in smarthphones

ACKNOWLEDGMENT

The authors express gratitude to the Facultad de Ingeniería of the Universidad Distrital Francisco José de Caldas, and also to the Dr. Paul T. Finger, MD.

REFERENCES

[1] K. Mahendraraj, S. Shrestha, C. S. M. Lau, and R. S. Chamberlain, "Ocular melanoma-when you have seen one, you have not seen them all: a clinical outcome study from the surveillance, epidemiology and end results (seer) database (1973-2012)," *Clinical Ophthalmology*, vol. 2017, no. 11, pp. 153-160, 2017.

[2] National Organization for Rare Disorders, "Rare disease database," 2019. [Online]. Available: https://rarediseases.org/rare-diseases/ocular-melanoma/. Accessed: September 2018.

[3] B. A. Krantz, N. Dave, K. M. Komatsubara, B. P. Marr, and R. D. Carvajal, "Uveal melanoma: epidemiology, etiology, and treatment of primary disease," *Clinical Ophthalmology*, vol. 2017, no. 11, pp. 279-289, 2017.
[4] P. Isager, G. Engholm, J. Overgaard, and H. Storm, "Uveal and conjunctival malignant melanoma in denmark 1943-1997 observed and relative survival of patients followed through 2002," *Ophthalmic Epidemiology*, vol. 13, no. 2, pp. 85-96, 2006.
[5] E. S. Blum, J. Yang, K. M. Komatsubara, and R. D. Carvajal, "Clinical management of uveal and conjunctival melanoma," *Oncology*, vol. 30, no. 1, pp. 29-32, 2016.
[6] Cancer.Net, "Eye cancer survival rates," ASC.org, 2015. [Online]. Available: https://www.cancer.org/cancer/eye-cancer/detection-diagnosisstaging/survival-rates.html#references. Accessed: September 2018.
[7] P. Nathan, V. Cohen, S. Coupland, and et al., "Uveal melanoma uk national guidelines," *European Journal of Cancer*, vol. 51, no. 16, pp. 2404-2412, 2015.
[8] M. Diener-West, S. M. Reynolds, D. J. Agugliaro, and et al., "Development of metastatic disease after enrollment in the coms trials for treatment of choroidal melanoma: Collaborative ocular melanoma study group report no. 26," *Archives of ophthalmology*, vol. 123, no. 12, pp. 1639-1643, 2005.
[9] M. A. Postow, D. Kuk, K. Bogatch, and R. D. Carvajal, "Assessment of overall survival from time of metastasis in mucosal, uveal, and cutaneous melanoma," *Journal of Clinical Oncology*, vol. 32, no. 15, 2014.
[10] P. Gupta, H. Mehrotra, A. Rattani, A. Chatterjee, and A. Kaushik, "Iris recognition using corner detection," *Proceedings of the 23rd International Biometric Conference,* Montreal Canada, 2006.
[11] J. Daugman, "Statistical richness of visual phase information: update on recognizing persons by iris patterns," *International Journal of Computer Vision*, vol. 45, no. 1, pp. 25-38, 2001.
[12] L. Flom and A. Safir, "Iris recognition system," 1987, U.S. Patent.
[13] P. Perner, "Iris acquisition and detection for computer-assisted iridiology," *IEEE 22nd Signal Processing and Communications Applications Conference*, 2014.
[14] S. Amerifar, A. T. Targhi, and M. M. Dehshibi, "Iris the picture of health: Towards medical diagnosis of diseases based on iris pattern," *The Tenth International Conference on Digital Information Management (ICDIM)*, 2015.
[15] F. Hernandez, R. Vega, F. Tapia, D. Morocho, and W. Fuertes, "Early detection of alzheimer's using digital image processing through iridology, an alternative method," *13th Iberian Conference on Information Systems and Technologies (CISTI)*, 2018.
[16] G. Durga Devi and D. Preethi, "Disease identification in iris using Gabor filter," *International Journal of Engineering and Computer Science*, vol. 3, pp. 5369-5399, 2014.
[17] A. Wibawa, M. A. R., Sitorus, and M. H. Purnomo, "Classification of iris image of patient chronic renal failure (crf) using watershed algorithm and support vector machine (svm)," *Journal of Theoretical and Applied Information Technology*, vol. 20, no. 20, pp. 1-9, 2016.
[18] W. Wei and Z. Jun, "Image encryption algorithm based on the key extracted from iris characteristics," *IEEE International Symposium on Computational Intelligence and Informatics*, 2013.
[19] R. P. Wildes, "Iris recognition: an emergin biometric technology," *Procedings of the IEEE*, vol. 85, no. 9, pp. 1348-1363, 1997.
[20] S. J. Kjeldgaard-Pedersen, "Circular hough transform," *Encyclopedia of Biometrics*, 2009.
[21] P. Roy, S. Dutta, N. Dey, G. Dey, S. Chakraborty, and R. Ray, "Adaptive thresholding: A comparative study," *International Conference on Control, Instrumentation, Communication and Computational Technologies (ICCICCT)*, 2014.
[22] F. Chaumette, "Image moments: A general and useful set of features for visual servoing," *IEEE Transactions on Robotics*, vol. 20, no. 4, pp. 713-723, 2004.
[23] H. Ming Kuei, "Visual pattern recognition by moment invariants," *IRE Transactions on Information Theory*, vol. 8, no. 2, pp. 179-187, 1962.
[24] M. R. Teaque, "Image analysis via the general theory of moments," *Journal of the Optical society of America*, vol. 70, no. 8, pp. 920-930, 1980.
[25] J. F. Boyce and W. J. Hossack, "Moment invariants for pattern recognition," *Pattern Recognition Letters*, vol. 1, pp. 451-456, 1983.
[26] Y. S. Abu-Mostafa and D. Psaltis, "Recognitive aspects of moments invariants," *IEEE Transactions on Pattern Analysis and Machine Intelligence*, vol. PAMI-6, no. 6, pp. 698-706, 1984.
[27] R. Mukundan and K. R. Ramakrishman, "Moment Functions in Image Analysis: Theory and Application," Singapore: World Scientific, 1998.
[28] R. J. Prokop and A. P. Reeves, "A survey of moment-based techniques for unoccluded object representation and recognition," *CVGIP: Graphical Models and Image Processing*, vol. 54, pp. 438-460, Sept 1992.
[29] Z. Huang and J. Leng, "Analysis of hu's moment invariants on image scaling and rotation," *Proceedings of 2nd International Conference on Computer Engineering and Technology (ICCET)*, vol. 7, 2010.
[30] R. C. Gonzales and R. E. Woods, "Digital Image Processing (Third Edition)," Prentice Hall, 2008.
[31] New York Eye Cancer Center, "Iris melanoma," 2018. [Online]. Available: https://eyecancer.com/eye-cancer/conditions/iris-tumors/irismelanoma. Accessed: September 2018.